https://doi.org/10.5194/egusphere-2026-6287
Preprint. Discussion started: 10 November 2026
© Author(s) 2026. CC BY 4.0 License.

Measurement Report: Lidar observations of Canadian wildfire smoke transported to East Asia in June 2025

Chuan Liu[1,2,3], Yun He[1,2,3*], Yue Jia[4*], Qiaoyun Hu[5], Zhenping Yin[6], Hao Yu[6], Feiyue Mao[6], Luhao Zuo[6], Zhaolong Wu[7], Dongzhe Jing[1,2,3], Tingyang Fu[1,2,3], Changming Yu[2,8], Kaiming Huang[1,2,3], Fan Yi[1,2,3]

[1]School of Earth and Space Science and Technology, Wuhan University, Wuhan 430072, China.
[2]National Field Observation and Research Station (Hubei Wuhan) for Atmospheric Remote Sensing, Wuhan 430072, China.
[3]Key Laboratory of Geospace Environment and Geodesy, Ministry of Education, Wuhan 430072, China.
[4]School of Natural Sciences and Mathematics, University of Texas at Dallas, Richardson 75080, USA.
[5]Univ. Lille, CNRS, UMR 8518 – LOA – Laboratoire d'Optique Atmosphérique, Villeneuve d'Ascq 59650, France.
[6]School of Remote Sensing and Information Engineering, Wuhan University, Wuhan 430072, China.
[7]Department of Atmospheric and Oceanic Sciences, School of Physics, Peking University, Beijing 100871, China.
[8]School of Electronic Information, Wuhan University, Wuhan 430072, China.

Correspondence to: Yun He (heyun@whu.edu.cn) and Yue Jia (yue.jia@utdallas.edu)

Abstract. This paper provides a timely measurement report on the vertical structures and optical properties of Canadian wildfire smoke over East Asia based on lidar observations at Wuhan and Beijing, China in early summer 2025. Ground-based lidars detected smoke layers over Wuhan (30.5°N, 114.4°E) and Beijing (40.0°N, 116.3°E), China, during 16-18 June. In Wuhan, two stratospheric smoke layers appeared at 16.0-16.7 km and 17.2-18.3 km, with particle extinction coefficients of 25.8 Mm^{-1} and 20.4 Mm^{-1}, raising stratospheric aerosol optical depth to 11.8 times the background level (0.052 versus 0.0044). The particle depolarization ratio (0.20) and lidar ratio (79±14 sr) at 532 nm indicate dominance of nonspherical, strongly absorptive smoke particles. In Beijing, a smoke layer appeared at 14.6-16.8 km, with a particle extinction coefficient of 47.7 Mm^{-1} and PDR of 0.17. China's DQ-1 spaceborne lidar captured the smoke plumes over East Asia, with a north-south horizontal extent of ~2800 km. MODIS and OMPS observations identified potential wildfire source regions in Canada, while FLEXPART dispersion simulations with observationally constrained release conditions indicated plausible transport pathways through Europe to East Asia. Our lidar observations provides valuable insights into the long-range transport and optical properties of North American wildfire smoke over East Asia in summer 2025.

https://doi.org/10.5194/egusphere-2026-6287
Preprint. Discussion started: 10 November 2026
© Author(s) 2026. CC BY 4.0 License.

1 Introduction

Wildfires release substantial amounts of smoke aerosols and trace gases into the atmosphere, significantly impacting regional climate, atmospheric chemistry, and human health. Furthermore, intense wildfires, particularly those associated with pyrocumulonimbus (pyroCb) events, are capable of lofting combustion products directly into the tropopause region and even the stratosphere (Peterson et al., 2017; Zhang et al., 2024). Once injected into the stratosphere, aerosols experience a marked increase in residence time, typically lasting from months to years, which allows them to be transported across continents over long distances and enables widespread influences on global radiative balance (Kremser et al., 2016) and stratospheric ozone chemistry (Trickl et al., 2015). In addition, smoke aerosols can act as ice-nucleating particles to trigger heterogeneous ice nucleation in cirrus clouds (Veselovskii et al., 2022; Mamouri et al., 2023; Ansmann et al., 2025).

Over the past decade, the intensity and frequency of wildfires have increased across North America, owing to changes in land cover, policy factors, and climate (Abatzoglou et al., 2019; UN, 2021; Seydi et al., 2025; Jain et al., 2024). This upward trend has led to more frequent and larger smoke particle injections into the upper troposphere and lower stratosphere (Ansmann et al., 2018; Hu et al., 2019, 2022; Khaykin et al., 2018; Trickl et al., 2024; Sakai et al., 2025; Fu et al., 2026). The long-range transport of smoke plumes and their potential impacts on the global atmosphere have attracted widespread attention, motivating extensive investigations into their transport pathways, spatio-temporal distribution, latitudinal reach across the Northern Hemisphere, optical and microphysical properties, and aging processes. The most intense and widely impacted North American wildfires took place in the summer (August) of 2017. During this event, Khaykin et al. (2018) found that lidar-observed stratospheric aerosol layers at Observatoire de Haute-Provence, France, can be traced back to several PyroCb clusters triggered by intense wildfires in northwest Canada and the United States; they found the smoke plumes had dispersed in the stratosphere across the Northern Hemisphere extratropics. For the same wildfire event, Ansmann et al. (2018) reported that the smoke plume split into at least two branches while crossing the eastern Atlantic, with one of them arriving in central Europe on 21-22 August 2017, resulting in an extremely high light extinction coefficient of 500 Mm^{-1}, as observed at three stations of European Aerosol Lidar Network (EARLINET) lidar, i.e., Hohenpeissenberg, Leipzig, and Kosetice. With the EARLINET observations, Baars et al. (2019) studied the decay phase and aerosol properties within 6 months following the wildfire outbreaks and found a decrease in the particle linear depolarization ratio over time, corresponding to smoke aging that changes particle shape to trend toward being spherical. The Canadian smoke plumes in summer 2017 were transported eastward even farther to the stratosphere over East Asia and twice passed over a further south site over central China, Wuhan (30.5°N), as captured by the Asian summer monsoon anticyclone (He et al., 2024).

Afterwards, North American wildfires occurred nearly every summer. In summer 2019, Shang et al. (2024) observed the evolution of wildfire-released smoke plumes transported from Canada across the North Atlantic to Europe. In summer 2023, Filonchyk and Peterson (2024) found that Canadian wildfire-released smoke possessed favorable meteorological conditions, i.e., cyclonic activity accompanied by large-scale transport from source regions across the Atlantic to Southern Europe. Hu et al. (2026) observed the long-range transported smoke layers from the 2023 Canadian wildfire using the dual-site Mie-Raman-polarization-fluorescence lidar observations in Lille, France, and Moscow, Russia, and compared the fluorescence magnitudes and spectral shapes, depolarization ratio, lidar ratio, and Ångström exponent of smoke aerosols at both sites. Notably, the 2023 Canadian wildfire smoke plumes followed distinct vertical transport pathways and only impacted mid- and high-latitudes (40°-70°N) of the Northern Hemisphere instead of even further south (Khaykin et al., 2025). In summer 2024, Joppe et al. (2025) observed elevated aerosol number concentrations in the tropopause region over Europe to be 2-4 times the background and can be tracked back to the emissions of Canadian wildfires via advective transport across the Atlantic and further lifting via the warm conveyor belt over Europe.

Our lidar site at Wuhan (30.5°N, 114.4°E) is located in a transition region between the tropics and midlatitudes over central China, which is further south than most lidar sites over the Northern Hemisphere; therefore, North American wildfire smoke does not always intrude into the stratosphere at such a southern location in summer. The most recent intrusion was

https://doi.org/10.5194/egusphere-2026-6287
Preprint. Discussion started: 10 November 2026
© Author(s) 2026. CC BY 4.0 License.

recorded in September and October 2017, which was related to the smoke released from the Canadian wildfire event in August 2017 (He et al., 2024). In summer 2025, a series of large-scale, intense wildfires occurred at the end of May in central Canada, which was much earlier than previous years, releasing massive smoke particles into the atmosphere and undergoing long-range transport to Europe within latitudes of 35°-53°N (Haarig et al., 2026). The smoke plumes moved southeastward farther to mainland China and were observed by our ground-based lidars at Wuhan at a latitude of 30°N, which has not been reported so far by lidar observations over East Asian elsewhere.

This 'Measurement Report' reports the wildfire smoke plumes originating transported from Canada to East Asia during late May and early June of 2025 by observations of multiple lidars at Wuhan and Beijing, China, with the aid of several spaceborne observations and particle dispersion simulations. The origin, transport pathways, spatio-temporal distribution, and optical properties of the smoke are characterized, providing the first-hand and valuable observational facts for further assessment of the environmental and climatic impact of released smoke in the wildfire season of 2015. The paper is organized as follows. Section 2 provides a concise description of the instruments and the associated data and modeling tools used. In Section 3, we present an overview of the 2025 Canadian wildfire episode, characterize the transport of the smoke plumes, and discuss the resulting features observed over China. Finally, Section 4 presents the summary and conclusions.

2 Instruments, Data, and Methodology

2.1 Lidar Observations in Wuhan

2.1.1 Polarization Lidar

In this study, we employed a ground-based 532-nm polarization lidar to detect smoke plumes over Wuhan (30.5°N, 114.4°E), located in central China. This lidar system was installed on the campus of Wuhan University in October 2010 and used for continuously observing the cloud/aerosol/precipitation profiles (Kong and Yi, 2015; Yi et al., 2021; Yin et al., 2021; He et al., 2022, 2026; Jing et al., 2025, 2026). Previous studies using this instrument have well characterized long-term variations in stratospheric aerosols (He et al., 2024) and captured specific events involving volcanic aerosols or wildfire smoke (Zhuang and Yi, 2016; Jing et al., 2023; Fu et al., 2026).

This lidar emits laser pulses with an energy of ~120 mJ at a repetition rate of 20 Hz. The receiver unit is equipped with a Cassegrain telescope with an effective aperture of 300 mm and a field-of-view of ~1 mrad. The detectors are photomultiplier tubes (PMTs) Hamamatsu 5783P, followed by a signal acquisition instrument, Licel TR40-160, which simultaneously collects the signals from each channel in analog mode (lower height) and in photon counting mode (upper height) (Zhang et al., 2014); they will subsequently be glued to a single profile, realizing at least 7 orders of magnitude dynamic range so that optically thin stratospheric aerosol layers can be identified. The raw data are collected with a temporal resolution of 1 min and a vertical resolution of 3.75 m (typically integrated to 30-m vertical bins for further analysis).

Particle backscatter coefficients (β_p) and particle extinction coefficients (α_p) are retrieved using the method from Fernald (1984). For the specific retrieval of optical properties of smoke particles, a constant lidar ratio of 70 sr (Haarig et al., 2018) was applied. In addition, the volume (molecule and particle) and particle linear polarization can also be obtained with the well-calibrated gain ratio K between perpendicular- and parallel-oriented channels (Freudenthaler et al., 2009). The details regarding the retrieval methodology and the associated uncertainties for aerosol optical parameters can be found in He et al. (2024).

2.1.2 Single-line-extracted pure rotational Raman (PRR) lidar

The PRR lidar employs an injection-seeded frequency-doubled Nd:YAG laser emitting at 532.237 nm, with a repetition rate of 30 Hz (Yi et al., 2024). The system comprises one transmitter and two independent receivers with telescope apertures of 1000 mm (for far field) and 300 mm (for near field), respectively. Each receiver has three detection channels, i.e., one elastic backscatter channel and two N_2 molecule PRR channels. Two Raman channels extract an anti-Stokes PRR single line of N_2

https://doi.org/10.5194/egusphere-2026-6287
Preprint. Discussion started: 10 November 2026
© Author(s) 2026. CC BY 4.0 License.

molecule with rotational quantum numbers J = 4 and J = 14, respectively, using a combination of a narrow band filter (with a full width at half maximum (FWHM) of ~0.16 nm) and a Fabry-Perot interferometer (FPI) (with a FWHM of ~30 pm).

The retrieval of temperature profiles from this PRR lidar can be found in detail in Weng et al. (2018) and Peng et al. (2021). By combining the Mie backscattering signal with two PRR signals, the particle backscatter and extinction coefficients, and thus the lidar ratio, can be analytically retrieved. The accurate aerosol lidar ratio retrieval helps confirm the presence of smoke aerosol that usually shows relatively larger values of approximately 65-100 sr compared with normal urban pollution and mineral dust (Müller et al., 2007; Haarig et al., 2025).

2.2 Lidar Observations in Beijing

In this study, we employed a ground-based micro pulse lidar (MPL) to detect smoke plumes over Beijing, located in northern China. The zenith-pointing MPL (model MPL-4B-IDS-532-AT, Sigma Space Corporation) has been operated continuously since 2016 on the rooftop of the west building of the School of Physics, Peking University (PKU; 40.0°N, 116.3°E; 40 m above sea level) (Chu et al., 2019; Xu et al., 2020; Wu et al., 2025, 2026a, b). The instrument is housed in a temperature-controlled enclosure beneath a slightly tilted protective window and a sun shield, enabling routine unattended observations. The MPL is an eye-safe, single-wavelength elastic polarization lidar operating at 532 nm. It transmits 6-8 μJ pulses at a repetition rate of 2500 Hz and has a receiver field of view of 0.1 mrad. An actively controlled liquid-crystal retarder alternates the polarization state, allowing the co- and cross-polarized components to be measured with a single detector (Flynn et al., 2007). The native temporal and vertical resolutions are 15 s and 15 m, respectively, and the near-range blind zone is approximately 195 m (Welton and Campbell, 2002).

The particle backscatter coefficient (βp) and particle extinction coefficient (αp) were retrieved from the elastic return at 532 nm using the Klett-Fernald inversion (Fernald, 1984). A constant aerosol lidar ratio of 70 sr was employed for smoke layers in the retrieval, consistent with the assumption for Wuhan's lidar observations (Haarig et al., 2018). The volume depolarization ratio was derived from the two polarization measurements, and the particle depolarization ratio was obtained after correcting for the molecular contribution (Freudenthaler et al., 2009).

2.3 FLEXible PARTicle (FLEXPART) dispersion model

The FLEXPART dispersion model (version 10.4; Pisso et al., 2019) was used to simulate the long-range transport of smoke aerosols from the 2025 Canadian wildfire events. FLEXPART is a Lagrangian particle dispersion model driven by three-dimensional meteorological fields, and it simulates atmospheric transport by calculating the trajectories of a large number of particles under the influence of resolved advection and parameterized turbulent diffusion. In this study, FLEXPART was driven by hourly ERA5 reanalysis meteorological data produced by the European Centre for Medium-Range Weather Forecasts (ECMWF; Hersbach et al., 2020). The ERA5 fields have a horizontal resolution of 1° × 1° and 137 vertical levels, providing the large-scale wind, temperature, pressure, and boundary layer information required for the transport simulations.

In our simulations, the released tracers were treated as passive particles, meaning that chemical transformation, dry and wet deposition, and gravitational settling were not included. Therefore, the simulated particle distributions represent the potential transport pathways and atmospheric residence of fine smoke aerosols, rather than the exact aerosol mass remaining after physical and chemical removal processes. This passive-tracer setup provides an upper-limit estimate of smoke persistence and downwind influence from the Canadian wildfire emissions. Daily model outputs, including particle positions and related meteorological parameters, were saved for subsequent analysis.

2.4 Ozone Mapping and Profiler Suite (OMPS) satellite

The OMPS is aboard the Suomi National Polar-orbiting Partnership (Suomi NPP) satellite (Jaross et al., 2014). It includes a limb profiler sensor. This sensor provides 510-nm aerosol extinction coefficient profiles. These profiles have a spatial

https://doi.org/10.5194/egusphere-2026-6287
Preprint. Discussion started: 10 November 2026
© Author(s) 2026. CC BY 4.0 License.

resolution of 5°×15° latitude-longitude grid. Each profile has a vertical resolution of 1 km, covering from the surface to an altitude of 40 km. OMPS also provides the stratospheric aerosol optical depth (sAOD) at 510 nm derived by integrating the aerosol extinction above the tropopause. In this study, we utilize the OMPS-NPP Level-3 monthly mean sAOD data from May to September 2025 to assess the further dispersion of smoke particles in the stratosphere of the Northern Hemisphere (Appendix A). These data allow the analysis of of smoke plume evolution in the stratosphere of the Northern Hemisphere.

We also used the OMPS ultraviolet Aerosol Index (AI) data, which reflect the absorptive properties of aerosols in the ultraviolet band. The AI is calculated from top-of-atmosphere radiance, which integrates the total aerosol effects (Hammer et al., 2018). It serves as an ideal indicator for tracking the evolution of episodic aerosol plumes from dust storms, volcanic ash, and biomass burning aerosols from fire events. In general, lower AI values correspond to clear skies associated with low aerosol loading.

2.5 Earth Cloud, Aerosol and Radiation Explorer (EarthCARE) spaceborne lidar

The EarthCARE satellite, launched in May 2024, is designed to provide global profiles of clouds, aerosols, and precipitation. It carries four scientific instruments, i.e., a 355-nm Atmospheric Lidar (ATLID), a 94-GHz Cloud Profiling Radar (CPR), a Multi-Spectral Imager (MSI), and a Broad-Band Radiometer (BBR) (Wehr et al., 2023). ATLID is a high-spectral-resolution lidar (HSRL) that measured the vertical distribution and optical properties (including vertically-resolved profiles of particle backscatter coefficient, extinction coefficient, depolarization ratio, and lidar ratio) of clouds and aerosols (van Zadelhoff et al., 2023), which is also useful in tracking and analyzing stratospheric aerosols (Khaykin et al., 2026). In this study, we used ATLID aerosol layer top data products to identify the altitude of smoke layers and determine whether these aerosols have entered the stratosphere. Besides, we also used the EarthCARE data to track the transport pathways and horizontal extension of the smoke plumes.

2.6 DQ-1 spaceborne lidar

The DQ-1 satellite, launched on 16 April 2022, is a Chinese atmospheric monitoring remote sensing mission. It carries an Aerosol and Carbon Detection Lidar (ACDL), which incorporates an HSRL module (Chen et al., 2023; Ke et al., 2022). The ACDL emits laser pulses at three wavelengths, i.e., at 532, 1064, and 1572 nm, with both depolarization and high-spectral-resolution detection at 532 nm, enabling the independent retrieval of height-resolved particle optical parameters and providing high-precision measurements of aerosols and clouds (Dai et al., 2024; Zha et al., 2024). To identify the smoke layers, we used the attenuated particle backscatter coefficient from the ACDL L2A data product and particle extinction coefficient and particle depolarization ratio from L2_05km_ACPro data, all of which have a horizontal resolution of 5 km and a vertical resolution of 24 m (Mao et al., 2025, 2026)

2.7 Moderate Resolution Imaging Spectroradiometer (MODIS) Measurements

The MODIS is a key instrument aboard both Terra and Aqua satellites, which form part of the National Aeronautics and Space Administration's (NASA) Earth Observing System. With a wide viewing swath of 2330 km, it provides near-global coverage on a daily basis. Its active fire detection algorithm operates by comparing the brightness temperature of candidate pixels with that of neighboring pixels in the 4-μm and 11-μm spectral channels. In this study, we used the MODIS Fire and Thermal Anomalies product (MCD14) derived from combined Terra and Aqua observations (Giglio and Justice, 2021a, 2021b) to identify the spatiotemporal distribution of wildfire hotspots over Canada during the last week of May 2025. In addition, daily true-color images from the MODIS instrument on Terra were used to verify the presence of smoke plumes during the initial days following emission.

https://doi.org/10.5194/egusphere-2026-6287
Preprint. Discussion started: 10 November 2026
© Author(s) 2026. CC BY 4.0 License.

3 Results and Discussions

3.1 Overview of Canadian wildfires near the source regions in the early summer of 2025

From mid-May 2025, the National Oceanic and Atmospheric Administration (NOAA) conducted continuous monitoring of wildfire-related heat signatures and dense smoke plumes across Canada under persistently hot, dry, and low atmospheric humidity conditions. Over the course of the wildfire season, more than 160 fires were reported nationwide, with the most intense activity concentrated mainly in Manitoba, Ontario, and Saskatchewan (https://www.nesdis.noaa.gov/news/noaa-satellites-monitor-canadian-wildfires-and-smoke, last access: 10 September 2026). By mid-August 2025, Canada had been experiencing a severe wildfire crisis, with cumulative burned area exceeding 7.3 million hectares, ranking as the second-worst wildfire season on national record, behind only the catastrophic 2023 season (https://canadaondemand.ca/canada-on-fire-how-2025-became-the-nations-second-worst-wildfire-season/, last access: 10 September 2026). These large wildfires generated strong convective updrafts, which rapidly filled the atmosphere over the source regions and surrounding areas with smoke.

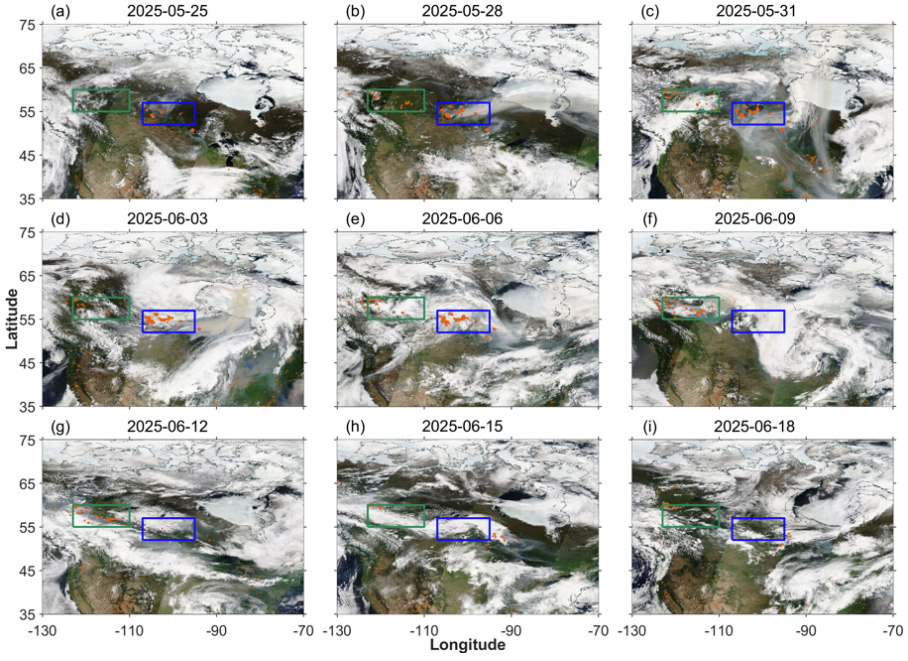


Figure 1: MODIS (Terra satellite) true-color images on 25, 28, 31 May, and 3, 6, 9, 12, 15, 18 June 2025, respectively, over North America. The spots of Aqua and Terra MODIS Fires and Thermal Anomalies (MCD14) are also shown with orange points. Region 1 (green rectangles, 55-60°N, 110-123°W) and Region 2 (blue rectangles, 52-57°N, 95-107°W) are two primary source regions.

Figure 1 presents MODIS true-color satellite images depicting wildfire hotspots over North America at the end of May and the beginning of June, in which one can identify and characterize the source regions of the smoke plumes. During this event, fire hotspots were mainly concentrated in two regions, i.e., Region 1 (55-60°N, 110-123°W; marked with green rectangles) and Region 2 (52-57°N, 95-107°W; marked with blue rectangles), which can be considered the primary burning areas. On 25 May, sporadic ignition spots (marked by orange points) first appeared in Region 2, associated with some small-scale visible smoke plumes. On 28 May, a large number of fire hotspots occurred in Region 2 with an easterly transported smoke plume; meanwhile, detectable fire activity began to be identified in Region 1. In both regions, ignition spots continued to be evident during 28-31 May; however, the fires in Region 2 seemed to be more intense than those in Region 1 according to the true-color image-identified smoke plumes. Therefore, Region 2 probably contributed a major part of transported smoke aerosols over the downwind regions afterwards. Since 31 May, smoke plumes began to transport farther southward to significantly influence the northeastern part of the United States. Fire activity subsequently declined, with a decrease in hotspot

https://doi.org/10.5194/egusphere-2026-6287
Preprint. Discussion started: 10 November 2026
© Author(s) 2026. CC BY 4.0 License.

counts in Region 1 after 15 June and in Region 2 after 9 June. After 15 June, smoke plumes were scarcely detectable, indicating a temporary lull for this wildfire event.

To further examine the relative contribution of released smoke in the two identified regions, we examined the OMPS ultraviolet aerosol index data from 25 May to 18 June 2025 are presented in Figure 2, and can reflect the presence of UV-absorbed smoke particles. As seen from AI values in Figure 2, it can be concluded that the wildfire events from Region 2 generally showed a more pronounced absorbing-aerosol signature during the observed period, which may undergo transcontinental transport and influence the farther downstream regions in the Northern Hemisphere. In general, in Region 2, the AI began to rise rapidly on 25 May, indicating substantial smoke particles released from the wildfires, which is consistent with the findings from the MODIS true-color images. On 31 May, the smoke plumes then underwent southeastward and northeastward transport successively, dispersing across northeastern America with AI values reaching and spreading further over Greenland and the European Arctic. From 12 June onward, the Region 2 associated AI gradually declined along with the extinction of fires, falling to below 1 by 18 June. In Region 1, the enhancement of AI only showed on 9 June, meaning that the contribution of smoke release from the end of May to the beginning of June is probably small.

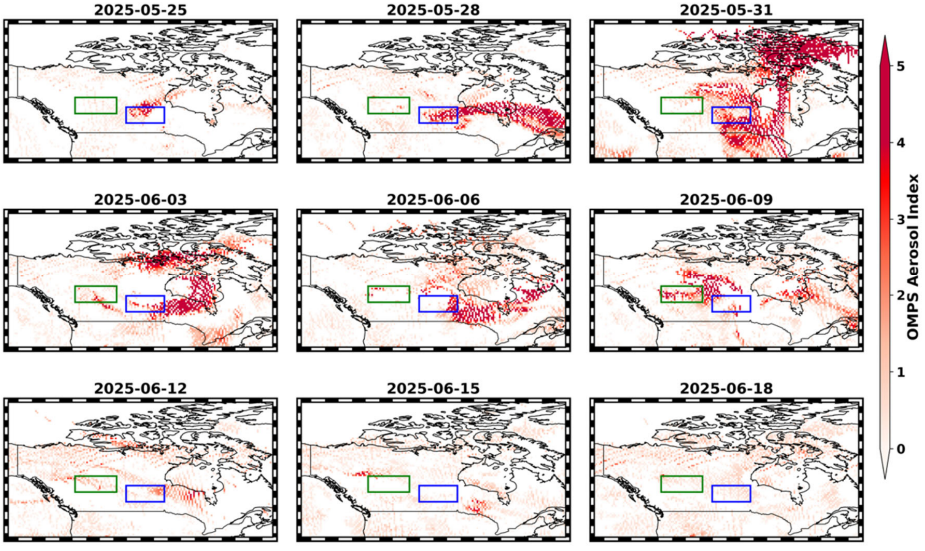


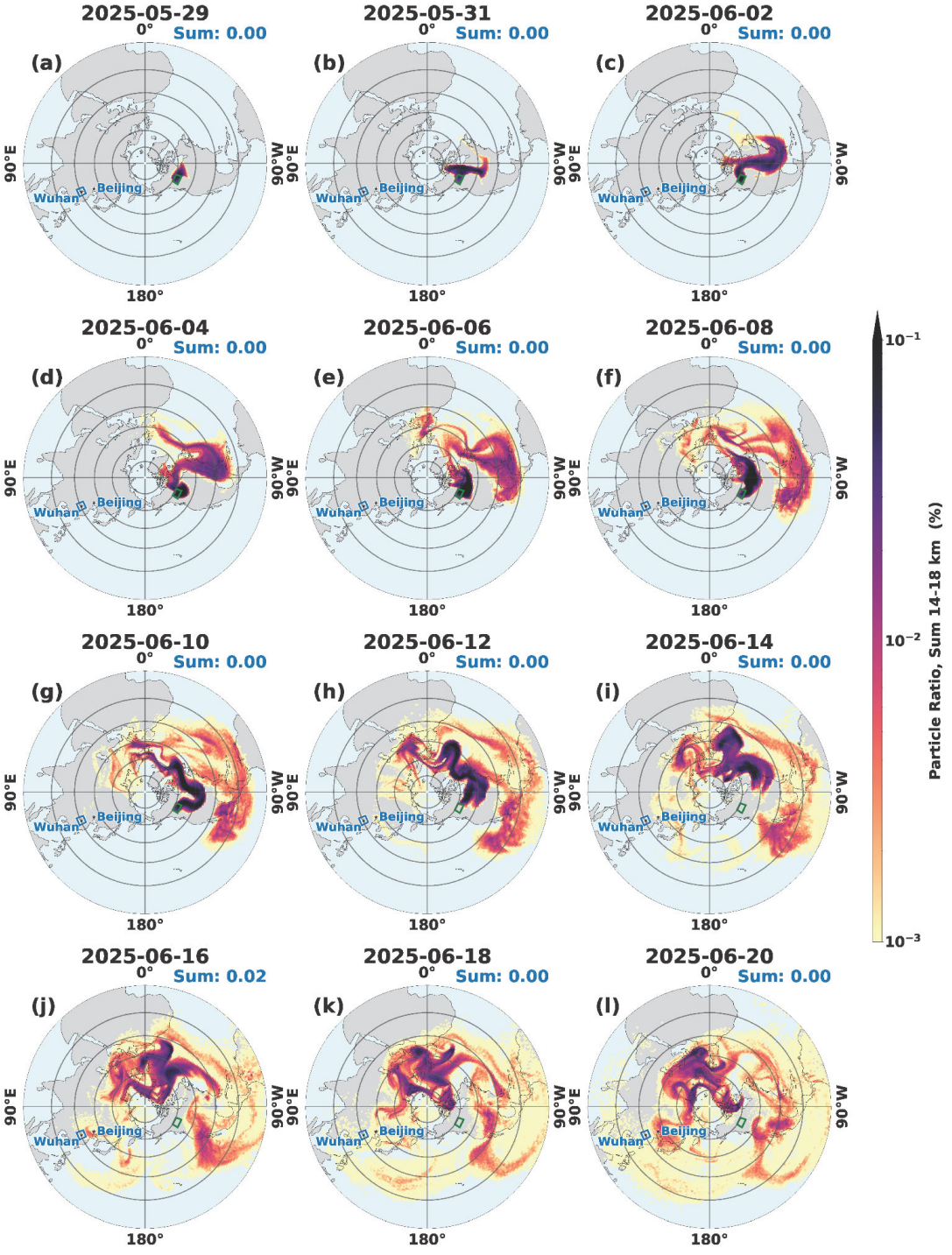
Figure 2: (a-i) OMPS Aerosol Index on 25, 28, 31 May, and 3, 6, 9, 12, 15, 18 June 2025, respectively, over North America. Region 1 (green rectangles; 55-60°N, 110-123°W) and Region 2 (blue rectangles; 52-57°N, 95-107°W) are two primary source regions.

3.2 Transport and horizontal extent of smoke plumes

To investigate the evolution and transport of the smoke aerosols, we conducted simulations using the FLEXPART Lagrangian particle dispersion model. The major challenge in representing wildfire smoke injection is that intense fires, particularly those associated with pyroCb convection, can rapidly loft smoke and combustion products into the upper troposphere and lower stratosphere (Peterson et al., 2017; Zhang et al., 2024), whereas the strong convective updrafts responsible for this vertical transport are not explicitly resolved by FLEXPART. Therefore, to address this issue, in the simulation we prescribed the particle release periods and altitudes based on the observed evolution of the stratospheric aerosol plume. The particle release periods were determined from the OMPS observations shown in Figure 2: particles were continuously released from Region 1 from 28 May to 10 June 2025 and from Region 2 from 25 May to 6 June 2025. For each source region, a total of 1 million particles were released uniformly over the corresponding release period. The initial height for the particle release was set to 14-18 km, which is generally consistent with the smoke aerosol layer-top heights observed by EarthCARE spaceborne lidar in Haarig et al. (2026). This prescribed-release approach allows the simulations to focus on

https://doi.org/10.5194/egusphere-2026-6287
Preprint. Discussion started: 10 November 2026
© Author(s) 2026. CC BY 4.0 License.

the subsequent large-scale transport and dispersion of smoke after its injection into the upper troposphere and lower stratosphere, while acknowledging uncertainty in the initial vertical injection process.



245 **Figure 3: The ratio of released particles (normalized by the total number released in the Canadian wildfire regions) within altitudes of 14-18 km, simulated for the selected Region 1 using the FLEXPART model. Wuhan was marked by a light blue box, and Beijing was marked by a black star. The red text indicates the sum of particle ratios within the red-outlined boxes near Wuhan.**

https://doi.org/10.5194/egusphere-2026-6287
Preprint. Discussion started: 10 November 2026
© Author(s) 2026. CC BY 4.0 License.

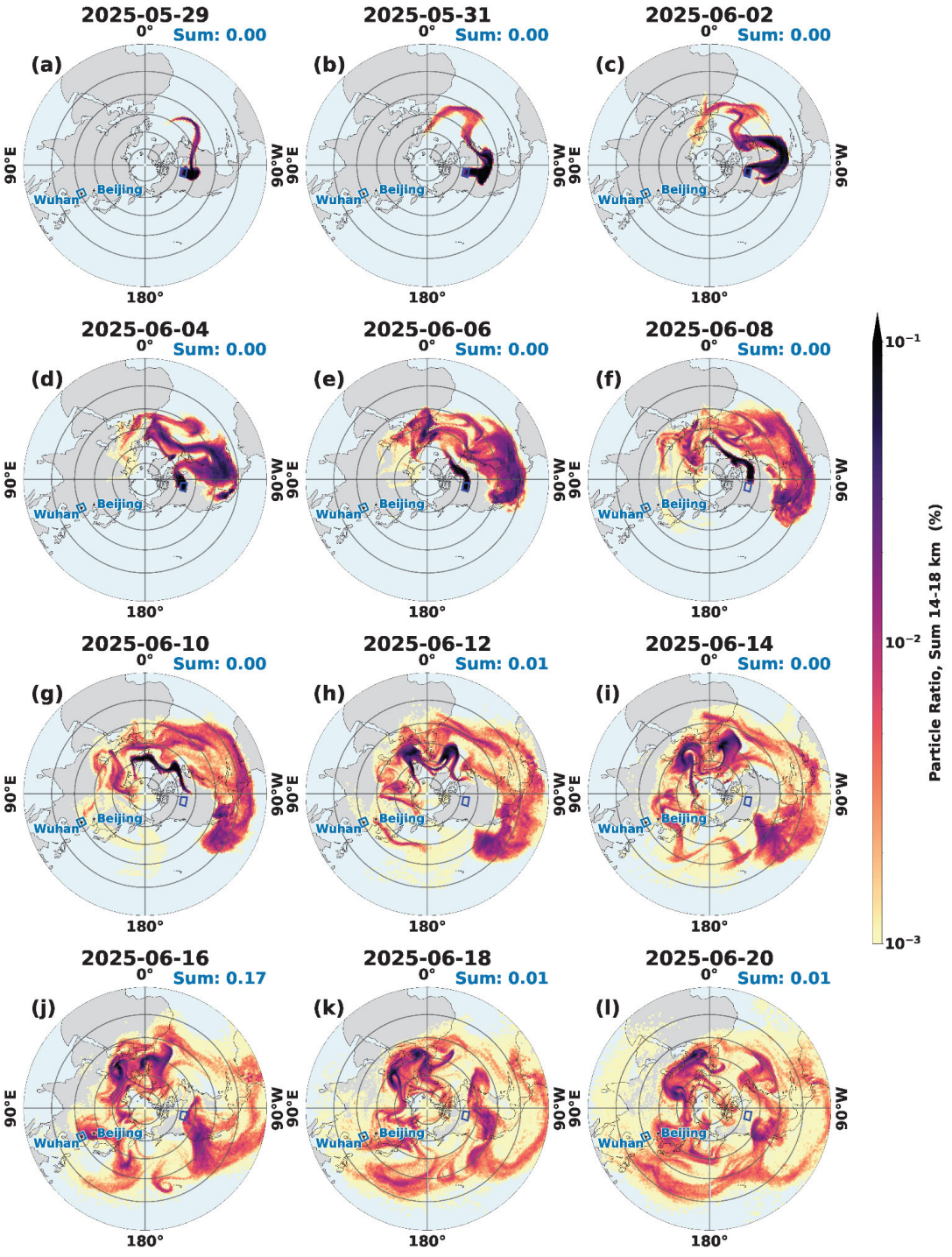


Figure 4: The ratio of released particles (normalized by the total number released in the Canadian wildfire regions) within altitudes of 14-18 km, simulated for the selected Region 2 using the FLEXPART model. Wuhan was marked by a light blue box, and Beijing was marked by a black star. The red text indicates the sum of particle ratios within the red-outlined boxes near Wuhan.

https://doi.org/10.5194/egusphere-2026-6287
Preprint. Discussion started: 10 November 2026
© Author(s) 2026. CC BY 4.0 License.

Figure 3 illustrates the spatial distribution of the percentage of released particles from Region 1. Initially, smoke aerosols were transported southward to central and northeastern America on 31 May. Subsequently, a portion of the smoke was gradually spread and persistently located within the tropics of North America and the Eastern Atlantic region in the following two weeks. Meanwhile, another portion of the smoke returned to high latitudes and began to transport northeastward on 2 June, reaching the European Arctic region by 4 June and continuing to advect into the middle- and high-latitude regions of Europe; afterwards, a limited portion of these smoke particles at high latitudes continued their eastward transport farther to Central Siberia, and then moved southeastward to enter China from Xinjiang Province, reaching Beijing on 14 June and Wuhan on 16 June, where we had ground-based lidar observations during the event. Moreover, after 16 June, smoke aerosols underwent a clockwise transport pathway and were brought from the western Pacific back to midlatitudes of mainland China, which was probably due to capture by the well-known Asian summer monsoon anticyclone (Wu et al., 2023).

Figure 4 displays the temporal evolution of the percentage of particles released from Region 2. Smoke aerosols from this region were transported eastward directly on 29 May and reached Europe by 31 May. A small fraction of these smoke particles continued eastward along with a similar transport pathway in Figure 3, with some traces arriving in Beijing on 8 June and Wuhan on 10 June, which were, however, too feeble to be detected by ground-based lidar observations at either site. In contrast, a more substantial portion (i.e., another branch of the smoke plume) of the smoke plume reached Wuhan during 16-18 June and showed a considerably higher particle ratio than those simulated on 12 June, which aligns well in time with the ground-based observations at Wuhan. Although the two source regions exhibited broadly similar transport pathways, particles originating from Region 2 generally diffused faster and more intensely. The simulation results further reveal that on 16 June, smoke aerosols formed a clockwise transport pathway over the mid-latitudes of East Asia with a hollow center structure, which may be associated with the horizontal barrier effect of the Asian summer monsoon anticyclone (Zhuang and Yi, 2016; Jing et al., 2023; He et al., 2024).

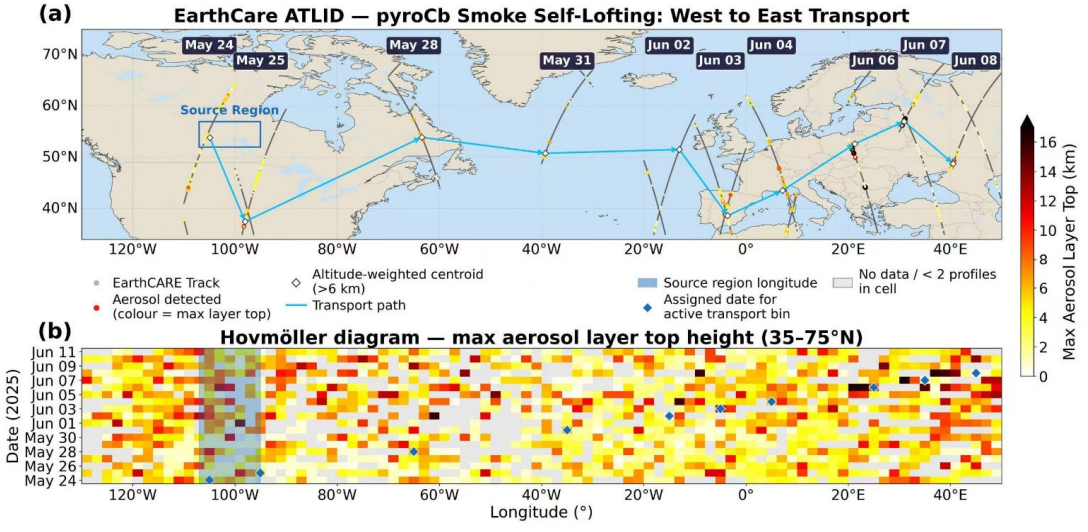


Figure 5: (a) EarthCARE footprints (from 24 May to 8 June, black curves) show the general transport pathway (light blue lines) of wildfire-induced smoke plumes from North America, across the Atlantic, to Europe. The source region is the area of 52-57°N, 95-107°W. The maximum aerosol layer tops are also shown for each satellite footprint. (b) Maximum aerosol layer top height varies with longitude (from 24 May to 11 June) as averaged for latitudes of 35-65°N.

In Figure 5, we used the EarthCARE ATLID lidar observations to track the smoke plume originating from Region 2. Spaceborne lidar measurements were more sensitive and initially detected the smoke signature on 24 May (one day earlier than MODIS observations as seen in Fig. 1), with maximum aerosol-layer top heights reaching approximately 4 km. On 25 May, the smoke plume first propagated southeastward, then veered northeastward before turning eastward across the North Atlantic, reaching Europe on 3 June at altitudes of approximately 10 km, which generally confirms the transport pathway as

https://doi.org/10.5194/egusphere-2026-6287
Preprint. Discussion started: 10 November 2026
© Author(s) 2026. CC BY 4.0 License.

simulated by the FLEXPART model and is consistent with the typical trans-Atlantic transport pathway of smoke plumes in the wildfire season of North America from other years (Wang et al., 2025). Upon arrival over Europe, the smoke plumes continued to move eastward, passing through Europe and subsequently extending into Central Asia, which is also reported by Haarig et al. (2026) based on HYSPLIT backward trajectory simulation.

3.3 Height-resolved optical properties of smoke aerosols transported to Wuhan and Beijing, China

Figure 6 shows the smoke plume observed over Wuhan by a 532-nm polarization lidar during 16-18 June 2025. The smoke particles initially appeared on the night of 16-17 June, exhibiting a double-layer structure generally located at altitudes of 16.0-16.7 km and 17.2-18.3 km, respectively, as indicated by both the enhancements of particle backscatter coefficient and volume depolarization ratio. During the night of 16-17 June, the lower-lying layer disappeared, while the upper layer persisted at slightly higher altitudes (17.9-18.8 km) than the night before and showed a gradual ascending trend. Note that the smoke layers persisted in the stratosphere of Wuhan (with a tropopause of around 14.8 km). During both nights, the particle backscatter coefficient within the smoke layer was mainly similar and situated at 0.3-0.4 $Mm^{-1}sr^{-1}$. It should also be mentioned that the significantly large particle backscatter coefficients together with higher PDR values of >0.3 below 13.5-km altitude are caused by cirrus clouds.

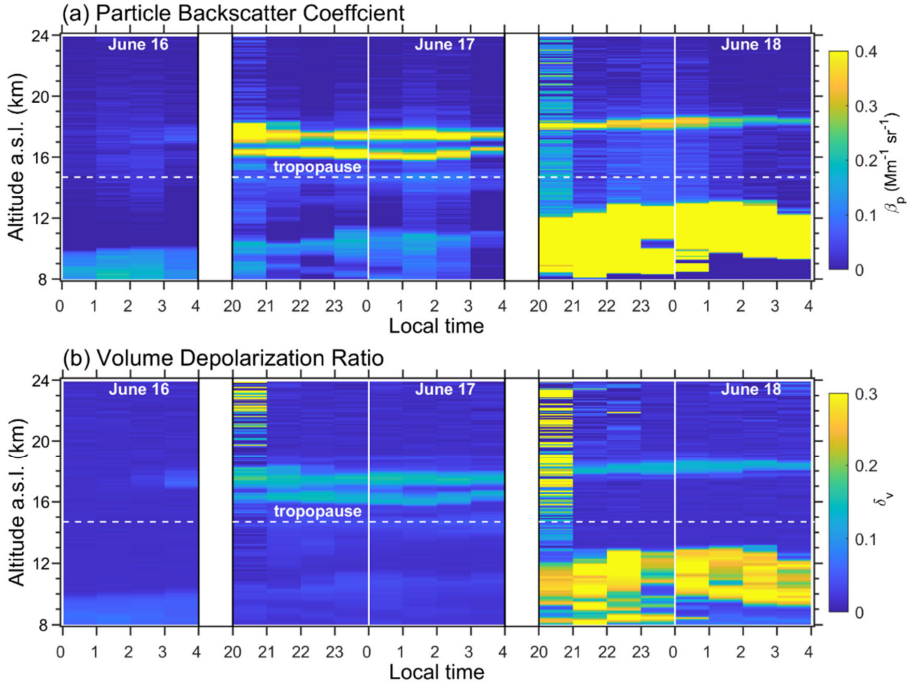


Figure 6: Time-height contour of one-hour integrated night-time (a) particle backscatter coefficient and (b) volume depolarization ratio measured by polarization lidar over Wuhan during 16-18 June 2025. White stripes represent daytime data with insufficient signal-to-noise ratio. White dashed lines indicate the altitudes of the tropopause calculated using temperature profiles from Wuhan's radiosonde measurements.

Figure 7 presents the profiles of particle backscatter coefficient, particle extinction coefficient, and particle depolarization ratio (PDR) based on 532-nm polarization lidar observations over Wuhan from 2000 LT to 2400 LT on 16 June (in red), and from 2300 LT on June 17 to 0230 LT on 17 June (in blue). During the first night, the layer-average particle extinction coefficient was 25.8±6.9 Mm^{-1} for the lower aerosol layer (at 16.0-16.7 km) and 20.4±6.7 Mm^{-1} for the upper aerosol layer (at 17.2-18.3 km), while the layer-average PDR value was 0.19±0.01 and 0.20±0.01, respectively. Note that both smoke layers

https://doi.org/10.5194/egusphere-2026-6287
Preprint. Discussion started: 10 November 2026
© Author(s) 2026. CC BY 4.0 License.

were located above the tropopause. During the second night, the smoke layer appeared at 17.9-18.8 km, with a layer-average particle extinction coefficient of 16.5±4.9 Mm^{-1} and a PDR value of 0.21±0.01. The sAOD (integrated from 1 km above the tropopause to 30-km altitude) was 0.052 during the night of 16-17 June and 0.026 during the night of 17-18 June, which are 11.8 times and 5.9 times the background sAOD level (0.0044±0.0019) at Wuhan observed during a stratosphere-quiescent period from January 2013 to August 2017 (He et al., 2024), indicating a pronounced stratospheric perturbation over Wuhan. In September and October 2017, we observed smoke plumes from intense Canadian wildfires with a similar level of plume-isolated AOD of 0.002-0.010 over Wuhan.

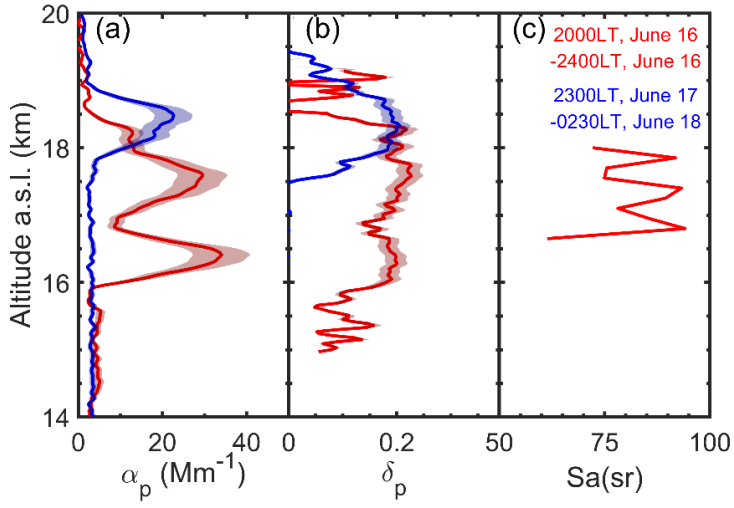


Figure 7: Lidar-derived profiles of (a) particle extinction coefficient, (b) particle depolarization ratio and (c) lidar ratio over Wuhan from 2000 LT to 2400 LT on 17 June (in red) and from 2300 LT on 17 June to 0230 LT on 18 June (in blue), respectively. The shaded area around each curve represents the uncertainty in the retrievals.

The PDR values (usually linked to a nonspherical particle shape) of smoke were as high as 0.19-0.21, which may have several potential explanations. In the 2017 Canadian wildfire event, Ansamnn et al. (2018) and Haarig et al. (2018) observed the PDRs for the long-range transported smoke in the stratosphere of Leipzig, Germany to be 0.18; they concluded that the smoke particles mostly uncoated, pure soot particles, since the lifting of convective cumulus towers was so fast to bring the released smoke to the tropopause region (within one hour), without allowing a sufficient residence time in the humid and aging-prone lower troposphere for any interactions with trace gases, other aerosol particles, or cloud drops. This can also be the case for the 2025 Canadian wildfire events. In addition, the lifting process of wildfire plumes may also impact the morphology of such smoke particles (Hu et al., 2026). According to in situ measurements, smoke particles injected into the upper troposphere and lower stratosphere (UTLS) region via PyroCb convection can exhibit distinctive characteristics, including enhanced particle sizes and even thicker organic coatings, compared with those without the linkage with such a strong convection process (Rosenfeld et al., 2007; Katich et al., 2023). The smoke particles with organic coatings may appear semi-solid and glassy in the UTLS region, which can be another potential explanation for the high PDR observed in Wuhan.

Figure 7d shows that the single-line-extracted PRR lidar measurement over Wuhan yielded the lidar ratios at 532 nm of 79±14 sr for the smoke layer at altitudes of 16.7-18.0 km (Peng et al., 2021; Yi et al., 2024), which are typical values representing fresh smoke aerosols enriched in absorptive black carbon (Ohneiser et al., 2020; Haarig et al., 2025). Lidar ratio generally reflects the nature of aerosols themselves regardless of aerosol loadings. Note that the aging process can result in a reduction in smoke lidar ratio to 40 sr (Hu et al., 2022) or 40-50 sr (Baars et al., 2021), and 44 sr (Sun et al., 2026), while hygroscopic growth may increase the lidar ratio of particles (Sun et al., 2026; Haarig et al., 2025). In August 2017, Haarig et al. (2018) observed the smoke layers from the Canadian wildfires over Leipzig, Germany, with smoke lidar ratios of 65-80 sr (66±12 sr) at 532nm. The smoke lidar ratios of 79±14 sr observed in this event were slightly larger than those observed by

https://doi.org/10.5194/egusphere-2026-6287
Preprint. Discussion started: 10 November 2026
© Author(s) 2026. CC BY 4.0 License.

Haarig et al. (2018). Considering that smoke particles were mainly transported within the stratosphere to Wuhan, it can be concluded that they had undergone neither a significant aging process nor hygroscopic growth during the transport, and the observed lidar ratio of 75-95 sr probably corresponded to the original feature of more absorptive smoke particles.

Figure 8 shows the optical properties of the smoke layer retrieved based on 532-nm ground-based lidar observations over Beijing (116°E, 40°N) during 0000-0300 LT on June 17. The smoke layer was mainly located at altitudes of 14.6-16.8 km, with the layer-average particle extinction coefficient of 47.7±20.6 Mm^{-1}, which is more than double the particle extinction observed over the further south site of Wuhan. This can be explained by the north-to-south transport pathway of the smoke plume over mainland China, as the smoke plume over the downstream Wuhan was further diluted along with transport and dispersion. The layer-average PDR was 0.17±0.02, with some differences between the upper and lower parts of the layer, suggesting that the aging level of the smoke particles exhibited some differences in the vertical direction, as also observed at several lidar sites of the China Aerosol Raman Lidar NETwork (CARLNET) (not shown here, Chen et al., 2026). The upper part of the smoke layer (14.8-16.8 km) mostly showed PDR values of 0.15-0.20 similar to those for fresh smoke; while the lower part (14.3-14.8 km) showed a partly aged characteristic with PDR values of 0.05-0.15. The tropopause over Beijing in summer is generally around an altitude of 15 km, meaning that the lower part (14.3-14.8 km) of the smoke layer may probably be located in the more humid, chemically active troposphere, which resulted in the partial aging of smoke particles there.

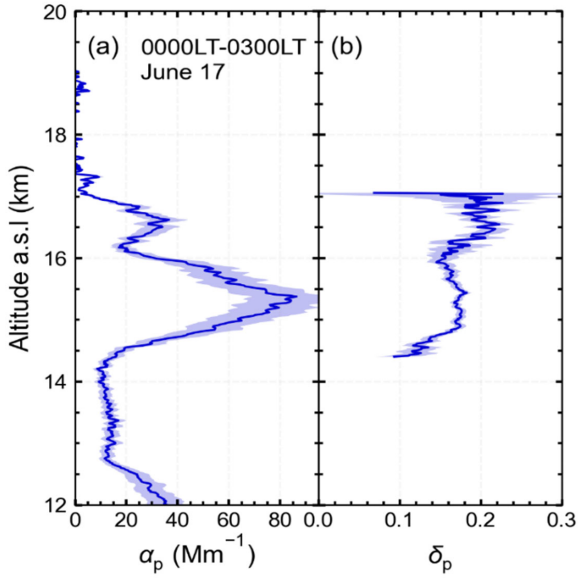


Figure 8: Lidar-derived profiles of (a) particle extinction coefficient, and (b) particle and volume depolarization ratio over Beijing during 0000-0300 LT on 17 June. The shaded area around each curve represents the uncertainty in the retrievals.

Figure 9a, b, and c display the 532-nm attenuated particle backscatter coefficient from the DQ-1 spaceborne lidar measurements on 16, 17, and 18 June 2025, respectively; their satellite footprints passed over mainland China, as shown in Figure 9d, with bold lines indicating the presence of detectable smoke. On 16 June, the smoke plume appeared at altitudes of approximately 17-19 km and extended over latitudes of 23-48° with a horizontal extent of 2800 km in East Asia. On 18 June, the smoke layer appeared slightly higher at altitudes of 18.5-19.8 km and became optically thinner below latitudes of 30°N, with a similar horizontal extent as on 16 June. The layer-average particle extinction coefficients were 26.7±20.0 Mm^{-1} on 16 June and 19.0±11.7 Mm^{-1} on 18 June. In general, PDR values within the smoke layer were vertically consistent around 0.13-0.16, reflecting the characteristics of slightly aged smoke particles.

https://doi.org/10.5194/egusphere-2026-6287
Preprint. Discussion started: 10 November 2026
© Author(s) 2026. CC BY 4.0 License.

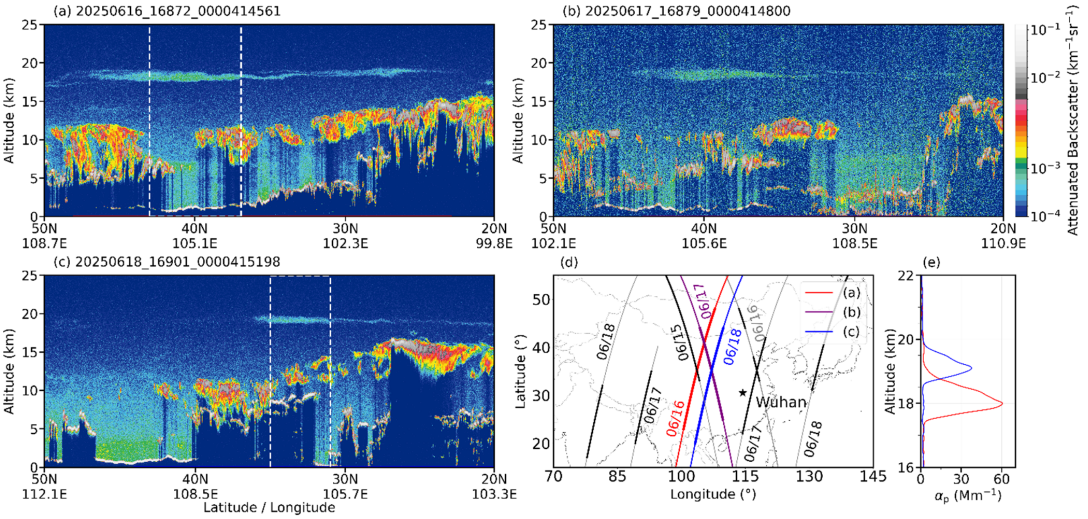


Figure 9: Attenuated backscatter at 532 nm from DQ1 spaceborne lidar observations with orbit numbers of (a) 16872_0000414561 on 16 June (nighttime), (b) 16879_0000414800 on 17 June (daytime), and (c) 16901_0000415198 on 18 June (nighttime). (d) DQ1 satellite footprints passing over East Asia during 16-18 June, with bold portions representing the inclusions of detectable smoke aerosols. The averaged profiles of (e) particle extinction coefficient are shown during the smoke presence periods in orbit (a) in red and (c) in blue.

4 Conclusions

Around the end of May 2025, a series of severe wildfire episodes occurred in Canada, releasing plenty of smoke aerosols into the atmosphere, subsequently initiating long-range transport across the Atlantic to Europe, and finally reaching East Asia. In this study, we took advantage of observations from several ground-based lidars deployed in Wuhan and Beijing, China, together with multiple spaceborne remote sensing instruments and the FLEXPART dispersion model to depict the origin, transport, vertical and horizontal distribution, and optical properties of smoke plumes in this event.

MODIS true-color images and OMPS aerosol index together identified two major smoke release regions, i.e., Region 1 (55-60°N, 110-123°W) started on 28 May, and Region 2 (52-57°N, 95-107°W) started earlier on 25 May. The fires in Region 2 are probably the major contributor to smoke aerosols. FLEXPART simulations and EarthCARE ATLID lidar measurements revealed the transport pathways of smoke plumes from the two identified source regions, across the North Atlantic to Europe. Smoke plumes from Region 2 were transported directly eastward on 29 May and reached Europe by 31 May; a major portion of smoke reached farther east to Wuhan and Beijing, China on 16-18 June, as confirmed by ground-based lidar observations. During 16-18 June, China's spaceborne lidar DQ-1 detected the smoke plumes at altitudes of 17-20 km over East Asia, with horizontal extents exceeding 2800 km.

Lidar observations at Wuhan, central China, captured the smoke layers in the stratosphere on 16-18 June. During the first night (16-17 June), two smoke layers appeared with layer-average particle extinction coefficients at 532 nm of 25.8±6.9 Mm^{-1} (lower layer at 16.0-16.7 km) and 20.4±6.7 Mm^{-1} (upper layer at 17.2-18.3 km); while the layer-average PDR at 532 nm was 0.19±0.01 and 0.20±0.01, respectively. During the second night (17-18 June), the upper layer slightly ascended to altitudes of 17.9-18.8 km, with a layer-average particle extinction coefficient of 16.5±4.9 Mm^{-1} and a PDR of 0.21±0.01. The sAOD was 0.052 and 0.026 during the two nights, nearly 12 times and 6 times the background sAOD level of 0.0044 over Wuhan, indicating a pronounced stratospheric perturbation. PDR values during both nights were around 0.20, possibly reflecting the dominance of irregular-shaped, non-coated particles similar to the characteristics of fresh smoke, or potentially PyroCb-convection-related organic coatings of smoke particles with semi-solid and glassy morphology. In addition, the lidar ratio of

https://doi.org/10.5194/egusphere-2026-6287
Preprint. Discussion started: 10 November 2026
© Author(s) 2026. CC BY 4.0 License.

smoke was 79±14 sr at 532 nm according to the observations by a pure rotational Raman lidar over Wuhan, which may depict the original feature of more absorptive smoke particles.

Lidar observation at Beijing indicated a lower smoke layer located around the UTLS region (14.6-16.8 km) on 17 June, associated with a layer-average particle extinction coefficient at 532nm of 47.7±20.6 Mm^{-1} and a PDR at 532 nm of 0.17±0.02. The upper part at 14.8-16.8 km included mostly fresh smoke particles (PDR=0.15-0.20), while the lower part at 14.3-14.8 km showed a partly aged characteristic (PDR=0.05-0.15), since this part may probably enter the more humid and chemically active troposphere, which is favorable for the particle aging process.

Our study showcases the capability of comprehensive analyses involving multiple passive and active spaceborne remote sensing observations, FLEXPART simulations, and ground-based lidar observations in monitoring the origin, transport, spatial and temporal distribution, and optical properties of wildfire-released smoke plumes, in particular after more than half a hemisphere's transport. Moreover, it is found that the North American wildfires not only become intense and frequent but also initiate much earlier in the summer of 2025, which should also be paid more attention to evaluate their impact on the regional atmospheric environment and even the environmental and climate influences over the downstream regions far from smoke sources. In addition, Europe already has the EARLINET (Baars et al., 2019), which has proven to be rather useful in wildfire smoke detection; thus, a large ground-based lidar network over East Asia (such as CARLNET, Shao et al., 2025; Chen et al., 2024) is also necessary and plays an essential role in monitoring such long-range transported smoke plumes from the wildfires of either North America or Siberia.

Appendix A

Figure A1 presents monthly mean sAOD from May to September 2025 observed by OMPS-NPP. In June, the sAOD values within latitudes of 40–80°N were significantly higher than those in other months, indicating much higher stratospheric aerosol injected by the Canadian wildfires at the end of May 2025. The sAOD enhancement suggests that smoke aerosols and their transport were predominantly confined to the stratosphere of the Northern Hemisphere at latitudes higher than 40°N. The maximum sAOD exceeded 0.04 in June. As a comparison, the maximum sAOD in the Northern Hemisphere during the 2017 Canadian wildfire event only reached 0.02, meaning that the fire intensity and smoke amount injected into the stratosphere are much greater in the summer of 2025 compared to the event in the summer of 2017 (He et al., 2024).

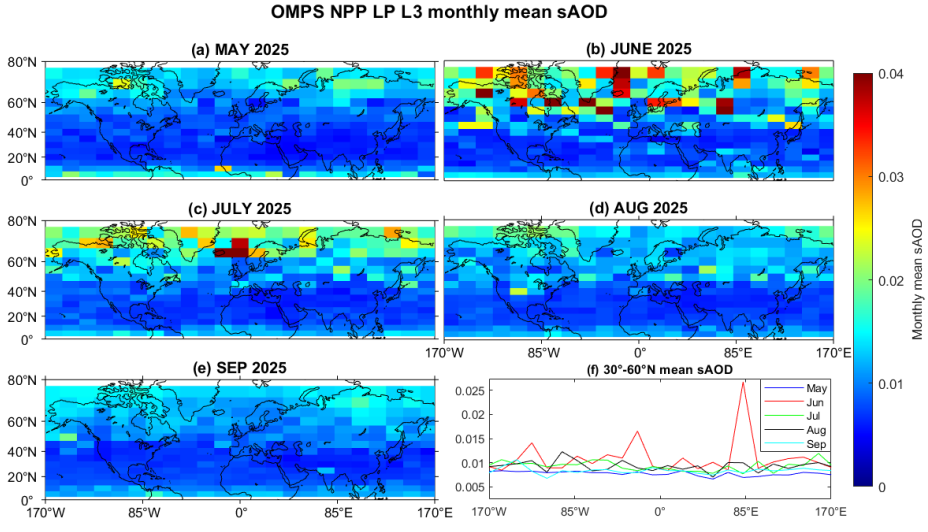


Figure A1: (a-e) OMPS-NPP Level-3 monthly mean sAOD at 510 nm from May to September 2025; (f) Monthly mean sAOD within latitudes of 30-60°N along longitude.

https://doi.org/10.5194/egusphere-2026-6287
Preprint. Discussion started: 10 November 2026
© Author(s) 2026. CC BY 4.0 License.

Data availability

The EarthCARE Level-2 demonstration products from simulated scenes, including the L1b data and the A-FM, A-PRO, and A-LAY products discussed in this paper, are available from https://earth.esa.int/eogateway/missions/earthcare/data (EarthCARE, 2026). MODIS images were taken from https://worldview.earthdata.nasa.gov (MODIS, 2026). The FLEXPART dispersion model (version 10.4) is available from https://www.flexpart.eu/. The OMPS data is available from https://search.earthdata.nasa.gov/search (OMPS, 2026). The ground-based lidar data and DQ-1 ACDL data are available via the link: https://doi.org/10.5281/zenodo.23319979 (He, 2026)

Author contributions

CL, YH, and YJ analyzed the data, conducted the investigations, and wrote the manuscript. YH, YJ, ZY, HY, QH, FM, and KH participated in scientific discussions, checked the results, and reviewed and proofread the manuscript. ZW, DJ, TF, CY, and LZ made efforts in retrieving the lidar-based aerosol optical properties. YH conceived the research and acquired the research funding. FY led the study.

Competing interests

The corresponding author has declared that none of the authors has any competing interests.

Acknowledgements

The authors thank the colleagues who participated in the operation of the lidar system at the Wuhan and Beijing sites. We also acknowledge NASA/NOAA for the OMPS data (https://www.earthdata.nasa.gov/sensors/omps/) and MODIS data (https://ladsweb.modaps.eosdis.nasa.gov/), the European Space Agency (ESA) and the Japan Aerospace Exploration Agency (JAXA) for the EarthCARE data, and the use of the FLEXPART Lagrangian particle dispersion model (https://www.flexpart.eu/) for simulating particle transport. Meteorological input was provided by the ERA5 reanalysis dataset from the ECMWF (https://www.ecmwf.int/en/forecasts/dataset/ecmwf-reanalysis-v5). We are grateful to the DQ-1 developing team for providing the ACDL spaceborne lidar data.

Financial support

This work was supported by the National Natural Science Foundation of China (grant nos. 42575138, 42575141), Hubei Provincial Special Project for Central Government Guidance on Local Science and Technology Development (2025CFC003), and the Meridian Space Weather Monitoring Project (China).

References

Abatzoglou, J. T., Williams, A. P., and Barbero, R.: Global emergence of anthropogenic climate change in fire weather indices, Geophys. Res. Lett., 46, 326–336, https://doi.org/10.1029/2018GL080959, 2019.

Ansmann, A., Baars, H., Chudnovsky, A., Mattis, I., Veselovskii, I., Haarig, M., Seifert, P., Engelmann, R., and Wandinger, U.: Extreme levels of Canadian wildfire smoke in the stratosphere over central Europe on 21–22 August 2017, Atmos. Chem. Phys., 18, 11831–11845, https://doi.org/10.5194/acp-18-11831-2018, 2018.

Ansmann, A., Jimenez, C., Roschke, J., Bühl, J., Ohneiser, K., Engelmann, R., Radenz, M., Griesche, H., Hofer, J., Althausen, D., Knopf, D. A., Dahlke, S., Gaudek, T., Seifert, P., and Wandinger, U.: Impact of wildfire smoke on Arctic cirrus

https://doi.org/10.5194/egusphere-2026-6287
Preprint. Discussion started: 10 November 2026
© Author(s) 2026. CC BY 4.0 License.

formation – Part 1: Analysis of MOSAiC 2019–2020 observations, Atmos. Chem. Phys., 25, 4847–4866, https://doi.org/10.5194/acp-25-4847-2025, 2025.

Baars, H., Ansmann, A., Ohneiser, K., Haarig, M., Engelmann, R., Althausen, D., Hanssen, I., Gausa, M., Pietruczuk, A., Szkop, A., Stachlewska, I. S., Wang, D., Reichardt, J., Skupin, A., Mattis, I., Trickl, T., Vogelmann, H., Navas-Guzmán, F., Haefele, A., Acheson, K., Ruth, A. A., Tatarov, B., Müller, D., Hu, Q., Podvin, T., Goloub, P., Veselovskii, I., Pietras, C., Haeffelin, M., Fréville, P., Sicard, M., Comerón, A., Fernández García, A. J., Molero Menéndez, F., Córdoba-Jabonero, C., Guerrero-Rascado, J. L., Alados-Arboledas, L., Bortoli, D., Costa, M. J., Dionisi, D., Liberti, G. L., Wang, X., Sannino, A., Papagiannopoulos, N., Boselli, A., Mona, L., D'Amico, G., Romano, S., Perrone, M. R., Belegante, L., Nicolae, D., Grigorov, I., Gialitaki, A., Amiridis, V., Soupiona, O., Papayannis, A., Mamouri, R.-E., Nisantzi, A., Heese, B., Hofer, J., Schechner, Y. Y., Wandinger, U., and Pappalardo, G.: The unprecedented 2017–2018 stratospheric smoke event: decay phase and aerosol properties observed with the EARLINET, Atmos. Chem. Phys., 19, 15183–15198, https://doi.org/10.5194/acp-19-15183-2019, 2019.

Baars, H., Radenz, M., Floutsi, A. A., Engelmann, R., Althausen, D., Heese, B., Ansmann, A., Flament, T., Dabas, A., Trapon, D., Reitebuch, O., Bley, S., and Wandinger, U.: Californian wildfire smoke over Europe: A first example of the aerosol observing capabilities of Aeolus compared to ground-based lidar, Geophys. Res. Lett., 48, https://doi.org/10.1029/2020GL092194, 2021.

Chen W., Liu J., Hou X., Zang H., Ma X., Wan Y., and Zhu X.: Lidar Technology for Atmosphere Environment Monitoring Satellite, Aerospace Shanghai (in Chinese), 40, 13–20, https://doi.org/10.19328/j.cnki.2096-8655.2023.03.002, 2023.

Chen, Y., Bu, Z., Wang, X., Dai, Y., Li, Z., Lu, T., Liu, Y., and Wang, X.: Development and Calibration of 532 nm Standard Aerosol Lidar with Low Blind Area, Remote Sens., 16, 570, https://doi.org/10.3390/rs16030570, 2024.

Chen, Y., Mao, S., Bu, Z., Dai, Y., Wang, X., Yin, Z., Müller, D., He, Y., Hu, Q., and Zhang, P.: Study on Canadian Wildfire Smoke Observed with China Aerosol Raman Lidar NETwork (CARLNET), Bull. Am. Meteorol. Soc., In revision, 2026.

Chu, Y., Li, J., Li, C., Tan, W., Su, T., and Li, J.: Seasonal and diurnal variability of planetary boundary layer height in Beijing: Intercomparison between MPL and WRF results, Atmos. Res., 227, 1–13, https://doi.org/10.1016/j.atmosres.2019.04.017, 2019.

Dai, G., Wu, S., Long, W., Liu, J., Xie, Y., Sun, K., Meng, F., Song, X., Huang, Z., and Chen, W.: Aerosol and cloud data processing and optical property retrieval algorithms for the spaceborne ACDL/DQ-1, Atmos. Meas. Tech., 17, 1879–1890, https://doi.org/10.5194/amt-17-1879-2024, 2024.

EarthCARE: Earth Cloud, Aerosol and Radiation Explorer, ESA [data set], https://earth.esa.int/eogateway/missions/earthcare/data, last access: 19 September 2026.

ERA5: ECMWF Reanalysis v5, ECMWF [data set], https://www.ecmwf.int/en/forecasts/dataset/ecmwf-reanalysis-v5, last access: 19 September 2026.

Fernald, F. G.: Analysis of atmospheric lidar observations: some comments, Appl. Optics, 23, 652–653, https://doi.org/10.1364/AO.23.000652, 1984.

Filonchyk, M., and Peterson, M. P.: Changes in aerosol properties at the El Arenosillo site in Southern Europe as a result of the 2023 Canadian forest fires, Environ. Res., 260, Article 119629, https://doi.org/10.1016/j.envres.2024.119629, 2024.

Flynn, C. J., Mendoza, A., Zheng, Y., and Mathur, S.: Novel polarization-sensitive micropulse lidar measurement technique, Opt. Express, 15, 2785-2790, https://doi.org/10.1364/OE.15.002785, 2007.

Freudenthaler, V., Esselborn, M., Wiegner, M., Heese, B., Tesche, M., Ansmann, A., Müller, D., Althausen, D., Wirth, M., Fix, A., Ehret, G., Knippertz, P., Toledano, C., Gasteiger, J., Garhammer, M., and Seefeldner, M.: Depolarization ratio profiling at several wavelengths in pure Saharan dust during SAMUM2006, Tellus B, 61, 165–179, https://doi.org/10.1111/j.1600-0889.2008.00396.x, 2009.

https://doi.org/10.5194/egusphere-2026-6287
Preprint. Discussion started: 10 November 2026
© Author(s) 2026. CC BY 4.0 License.



Fu, T., He, Y., Jia, Y., Jing, D., and Yi, F.: Lidar observations of optical properties of two upper troposphere and lower stratosphere aerosol plumes at Wuhan, Atmos. Res., 327, 108347, https://doi.org/10.1016/j.atmosres.2025.108347, 2026.

Giglio, L., Justice, C.: MODIS/Aqua Thermal Anomalies/Fire 5-Min L2 Swath 1km V061 [Dataset]. NASA Land Processes Distributed Active Archive Center. https://doi.org/10.5067/MODIS/MYD14.061, 2021a.

Giglio, L., Justice, C.: MODIS/Terra Thermal Anomalies/Fire 5-Min L2 Swath 1km V061 [Dataset]. NASA Land Processes Distributed Active Archive Center. https://doi.org/10.5067/MODIS/MOD14.061, 2021b.

Haarig, M., Ansmann, A., Baars, H., Jimenez, C., Veselovskii, I., Engelmann, R., and Althausen, D.: Depolarization and lidar ratios at 355, 532, and 1064 nm and microphysical properties of aged tropospheric and stratospheric Canadian wildfire smoke, Atmos. Chem. Phys., 18, 11847–11861, https://doi.org/10.5194/acp-18-11847-2018, 2018.

Haarig, M., Engelmann, R., Baars, H., Gast, B., Althausen, D., and Ansmann, A.: Discussion of the spectral slope of the lidar ratio between 355 and 1064 nm from multiwavelength Raman lidar observations, Atmos. Chem. Phys., 25, 7741–7763, https://doi.org/10.5194/acp-25-7741-2025, 2025.

Haarig, M., Baars, H., König, L., Donovan, D. P., Ansmann, A., Khaykin, S., Ceolato, R., Gast, B., Jimenez, C., Floutsi, A., Hogan, R., Chantry, A., Marnas, F., Roschke, J., van Zadelhoff, G.J., and Wandinger, U.: The life cycle of a stratospheric smoke plume as seen from EarthCARE—tracking a plume from Canada to Europe. Geophys. Res. Lett., 53, e2025GL119977, https://doi.org/10.1029/2025GL119977, 2026.

Hammer, M. S., Martin, R. V., Li, C., Torres, O., Manning, M., and Boys, B. L.: Insight into global trends in aerosol composition from 2005 to 2015 inferred from the OMI Ultraviolet Aerosol Index, Atmos. Chem. Phys., 18, 8097–8112, https://doi.org/10.5194/acp-18-8097-2018, 2018.

He, Y., Yi, F., Yin, Z., Liu, F., Yi, Y., and Zhou, J.: Mega Asian dust event over China on 27–31 March 2021 observed with space-borne instruments and ground-based polarization lidar, Atmos. Environ., 285, 119238, https://doi.org/10.1016/j.atmosenv.2022.119238, 2022.

He, Y., Jing, D., Yin, Z., Ohneiser, K., and Yi, F.: Long-term (2010–2021) lidar observations of stratospheric aerosols in Wuhan, China, Atmos. Chem. Phys., 24, 11431–11450, https://doi.org/10.5194/acp-24-11431-2024, 2024.

He, Y., Jing, D., Yin, Z., Müller, D., Liu, F., Zhang, Y., Yi, Y., Huang, K., and Yi, F.: Hygroscopic growth obscures actual variation in anthropogenic aerosol optical depth over central China during 2010–2024, Atmos. Chem. Phys., 26, 4937–4951, https://doi.org/10.5194/acp-26-4937-2026, 2026.

He, Y.: Measurement Report: Canadian wildfire smoke aerosols transport over long distance to East Asia in June 2025 as revealed with multiple spaceborne measurements, FLEXPART dispersion simulations, and ground-based lidar observations (Version V1) [Dataset]. Zenodo. https://doi.org/10.5281/zenodo.23319979, 2026.

Hersbach, H., Bell, B., Berrisford, P., Hirahara, H., Horányi, A., Muñoz-Sabater, J., Nicolas, J., Peubey, C., Radu, R., Schepers, D., Simmons, A., Soci, C., Abdalla, S., Abellan, X., Balsamo, G., Bechtold, P., Biavati, G., Bidlot, J., Bonavita, M., Chiara, G.D., Dahlgren, P., Dee, D., Diamantakis, M., Dragani, R., Flemming, J., Forbes, R., Fuentes, M., Geer, A., Haimberger, L., Healy, S., Hogan, R.J., Hólm, E., Janisková, M., Keeley, S., Laloyaux, P., Lopez, P., Lupu, C., Radnoti, G., Rosnay, P., Rozum, I., Vamborg, F., Villaume, S., Thépaut, J.N.: The ERA5 global reanalysis. Q J R Meteorol Soc. 2020; 146: 1999–2049. https://doi.org/10.1002/qj.3803, 2020.

Hu, Q., Goloub, P., Veselovskii, I., Bravo-Aranda, J.-A., Popovici, I. E., Podvin, T., Haeffelin, M., Lopatin, A., Dubovik, O., Pietras, C., Huang, X., Torres, B., and Chen, C.: Long-range-transported Canadian smoke plumes in the lower stratosphere over northern France, Atmos. Chem. Phys., 19, 1173–1193, https://doi.org/10.5194/acp-19-1173-2019, 2019.

Hu, Q., Goloub, P., Veselovskii, I., and Podvin, T.: The characterization of long-range transported North American biomass burning plumes: what can a multi-wavelength Mie–Raman-polarization-fluorescence lidar provide?, Atmos. Chem. Phys., 22, 5399–5414, https://doi.org/10.5194/acp-22-5399-2022, 2022.

https://doi.org/10.5194/egusphere-2026-6287
Preprint. Discussion started: 10 November 2026
© Author(s) 2026. CC BY 4.0 License.



Hu, Q., Goloub, P., Veselovskii, I., Podvin, T., Dubois, G., Khaykin, S., Boissière, W., Ducos, F., and Korenskiy, M.: Advanced insights into biomass burning aerosols during the 2023 Canadian wildfires from dual-site Raman and fluorescence lidar observations, Atmos. Chem. Phys., 26, 13027–13053, https://doi.org/10.5194/acp-26-13027-2026, 2026.

Jain, P., Barber, Q. E., Taylor, S. W., Whitman, E., Castellanos Acuna, D., Boulanger, Y., Chavardès, R. D., Chen, J., Englefield, P., Flannigan, M., Girardin, M. P., Hanes, C. C., Little, J., Morrison, K., Skakun, R. S., Thompson, D. K., Wang, X., and Parisien, M.-A.: Drivers and Impacts of the Record-Breaking 2023 Wildfire Season in Canada, Nat. Commun., 15, 6764, https://doi.org/10.1038/s41467-024-51154-7, 2024.

Jaross, G., Bhartia, P. K., Chen, G., Kowitt, M., Haken, M., Chen, Z., Xu P., Warner, J., and Kelly, T.: OMPS Limb Profiler instrument performance assessment. J. Geophys. Res.-Atmos., 119, 4399–4412, https://doi.org/10.1002/2013JD020482, 2014.

Jing, D., He, Y., Yin, Z., Liu, F., Yi, Y., and Yi, F.: Evolution of aerosol plumes from 2019 Raikoke volcanic eruption observed with polarization lidar over central China, Atmos. Environ., 309, 119880, https://doi.org/10.1016/j.atmosenv.2023.119880, 2023.

Jing, D., He, Y., Yin, Z., Huang, K., Liu, F., and Yi, F.: Evolution of tropospheric aerosols over central China during 2010–2024 as observed by lidar, Atmos. Chem. Phys., 25, 17047–17067, https://doi.org/10.5194/acp-25-17047-2025, 2025.

Jing, D., He, Y., Yin, Z., Müller, D., Huang, K., and Yi, F.: Hygroscopic growth characteristics of anthropogenic aerosols over central China revealed by lidar observations, Atmos. Meas. Tech., 19, 389–403, https://doi.org/10.5194/amt-19-389-2026, 2026.

Joppe, P., Schneider, J., Wilsch, J., Bozem, H., Breuninger, A., Curtius, J., Ebert, M., Emig, N., Hoor, P., Ismayil, S., Kandler, K., Kunkel, D., Kurth, I., Lachnitt, H.-C., Li, Y., Miltenberger, A., Richter, S., Rolf, C., Schneider, L., Schwenk, C., Spelten, N., Vogel, A. L., Cheng, Y., and Borrmann, S.: Transport of Biomass Burning Aerosol into the Extratropical Tropopause Region over Europe via Warm Conveyor Belt Uplift, Atmos. Chem. Phys., 25, 15077–15103, https://doi.org/10.5194/acp-25-15077-2025, 2025.

Katich, J. M., Apel, E. C., Bourgeois, I., Brock, C. A., Bui, T. P., Campuzano-Jost, P., Commane, R., Daube, B., Dollner, M., Fromm, M., Froyd, K. D., Hills, A. J., Hornbrook, R. S., Jimenez, J. L., Kupc, A., Lamb, K. D., McKain, K., Moore, F., Murphy, D. M., Nault, B. A., Peischl, J., Perring, A. E., Peterson, D. A., Ray, E. A., Rosenlof, K. H., Ryerson, T., Schill, G. P., Schroder, J. C., Weinzierl, B., Thompson, C., Williamson, C. J., Wofsy, S. C., Yu, P., and Schwarz, J. P.: Pyrocumulonimbus affect average stratospheric aerosol composition, Science, 379, 815–820, https://doi.org/10.1126/science.add3101, 2023.

Ke, J., Sun, Y., Dong, C., Zhang, X., Wang, Z., Lyu, L., Zhu, W., Ansmann, A., Su, L., Bu, L., Xiao, D., Wang, S., Chen, S., Liu, J., Chen, W., Liu, D.: Development of China's first space-borne aerosol-cloud high-spectral-resolution lidar: retrieval algorithm and airborne demonstration. PhotoniX, 3, 17, https://doi.org/10.1186/s43074-022-00063-3, 2022.

Khaykin, S. M., Godin-Beekmann, S., Hauchecorne, A., Pelon, J., Ravetta, F., and Keckhut, P.: Stratospheric smoke with unprecedentedly high backscatter observed by lidars above southern France, Geophys. Res. Lett., 45, 1639–1646, https://doi.org/10.1002/2017GL076763, 2018.

Khaykin, S., Bekki, S., Godin-Beekmann, S., Fromm, M. D., Goloub, P., Hu, Q., Josse, B., Laeng, A., Meziane, M., Peterson, D. A., Pelletier, S., and Thouret, V.: Stratospheric impact of the anomalous 2023 Canadian wildfires: the two vertical pathways of smoke, Atmos. Chem. Phys., 25, 14551–14571, https://doi.org/10.5194/acp-25-14551-2025, 2025.

Khaykin, S., Sicard, M., Leblanc, T., Sakai, T., Balugin, N., Berthet, G., Chevrier, S., Chouza, F., Feofilov, A., Gantois, D., Godin-Beekmann, S., Haddouche, A., Jin, Y., Morino, I., Kadygrov, N., Lecas, T., Liley, B., Querel, R., Taha, G., and Yushkov, V.: Global transport of stratospheric aerosol produced by Ruang eruption from EarthCARE ATLID, limb-

https://doi.org/10.5194/egusphere-2026-6287
Preprint. Discussion started: 10 November 2026
© Author(s) 2026. CC BY 4.0 License.

viewing satellites and ground-based lidar observations, Atmos. Chem. Phys., 26, 607–622, https://doi.org/10.5194/acp-26-607-2026, 2026.

Kong, W. and Yi, F.: Convective boundary layer evolution from lidar backscatter and its relationship with surface aerosol concentration at a location of a central China megacity, J. Geophys. Res.-Atmos., 120, 7928–7940, https://doi.org/10.1002/2015JD023248, 2015.

Kremser, S., Thomason, L., von Hobe, M., Hermann, M., Deshler, T., Timmreck, C., Toohey, M., Stenke, A., Schwarz, J., Weigel, R., Fueglistaler, S., Prata, F., Vernier, J., Schlager, H., Barnes, J., Antũna-Marrero, J., Fairlie, D., Palm, M., Mahieu, E., Notholt, J., Rex, M., Bingen, C., Vanhellemont, F., Bourassa, A., Plane, J., Klocke, D., Carn, S., Clarisse, L., Trickl, T., Neely, R., James, A., Rieger, L., Wilson, J., Meland, B.: Stratospheric aerosol–Observations, processes, and impact on climate, Rev. Geophys., 54, 278–335. https://doi.org/10.1002/2015RG000511, 2016.

Mamouri, R.-E., Ansmann, A., Ohneiser, K., Knopf, D. A., Nisantzi, A., Bühl, J., Engelmann, R., Skupin, A., Seifert, P., Baars, H., Ene, D., Wandinger, U., and Hadjimitsis, D.: Wildfire smoke triggers cirrus formation: lidar observations over the eastern Mediterranean, Atmos. Chem. Phys., 23, 14097–14114, https://doi.org/10.5194/acp-23-14097-2023, 2023.

Mao, F., Xu, W., Pan, Z., Zang, L., Han, G., Dai, L., Hu, X., Chen, W., Gong, W.: Aerosol-cloud layer detection algorithm of the DQ-1/ACDL, Remote Sens. Environ., 332, 115068, https://doi.org/10.1016/j.rse.2025.115068, 2025

Mao, F., Li, C., Zang, L., Pan, Z., Xu, W., Han, G., Hu, X., Chen, W., Gong, W.: Linear-Fitting calibration algorithm for Aerosol-Cloud detection channels at 532 nm of the DQ-1/ACDL, Int. J. Appl. Earth Obs. Geoinf., 153, 105504, https://doi.org/10.1016/j.jag.2026.105504, 2026.

MODIS: Moderate Resolution Imaging Spectroradiometer, NASA Worldview [data set], https://worldview.earthdata.nasa.gov, last access: 19 September 2026.

Müller, D., Ansmann, A., Mattis, I., Tesche, M., Wandinger, U., Althausen, D., and Pisani, G.: Aerosol-type-dependent lidar ratios observed with Raman lidar, J. Geophys. Res.-Atmos., 112, D16202, https://doi.org/10.1029/2006JD008292, 2007.

Ohneiser, K., Ansmann, A., Baars, H., Seifert, P., Barja, B., Jimenez, C., Radenz, M., Teisseire, A., Floutsi, A., Haarig, M., Foth, A., Chudnovsky, A., Engelmann, R., Zamorano, F., Bühl, J., and Wandinger, U.: Smoke of extreme Australian bushfires observed in the stratosphere over Punta Arenas, Chile, in January 2020: optical thickness, lidar ratios, and depolarization ratios at 355 and 532 nm, Atmos. Chem. Phys., 20, 8003–8015, https://doi.org/10.5194/acp-20-8003-2020, 2020.

Ohneiser, K., Ansmann, A., Witthuhn, J., Deneke, H., Chudnovsky, A., Walter, G., and Senf, F.: Self-lofting of wildfire smoke in the troposphere and stratosphere: simulations and space lidar observations, Atmos. Chem. Phys., 23, 2901–2925, https://doi.org/10.5194/acp-23-2901-2023, 2023.

OMPS: Ozone Mapping and Profiler Suite, NASA/NOAA [data set], https://www.earthdata.nasa.gov/sensors/omps/, last access: 19 September 2026.

Peng, L., Yi, F., Liu, F., Yin, Z., and He Y.: Optical properties of aerosol and cloud particles measured by a single-line-extracted pure rotational Raman lidar, Opt. Express 29, 21947–21964, https://doi.org/10.1364/OE.427864, 2021.

Peterson, D. A., Hyer, E. J., Campbell, J. R., Solbrig, J. E., and Fromm, M. D.: A Conceptual Model for Development of Intense Pyrocumulonimbus in Western North America, Mon. Weather Rev., 145, 2235–2255, https://doi.org/10.1175/MWR-D-16-0232.1, 2017.

Pisso, I., Sollum, E., Grythe, H., Kristiansen, N. I., Cassiani, M., Eckhardt, S., Arnold, D., Morton, D., Thompson, R. L., Groot Zwaaftink, C. D., Evangeliou, N., Sodemann, H., Haimberger, L., Henne, S., Brunner, D., Burkhart, J. F., Fouilloux, A., Brioude, J., Philipp, A., Seibert, P., and Stohl, A.: The Lagrangian particle dispersion model FLEXPART version 10.4, Geosci. Model Dev., 12, 4955–4997, https://doi.org/10.5194/gmd-12-4955-2019, 2019.

https://doi.org/10.5194/egusphere-2026-6287
Preprint. Discussion started: 10 November 2026
© Author(s) 2026. CC BY 4.0 License.

Rosenfeld, D., Fromm, M., Trentmann, J., Luderer, G., Andreae, M. O., and Servranckx, R.: The Chisholm firestorm: observed microstructure, precipitation and lightning activity of a pyro-cumulonimbus, Atmos. Chem. Phys., 7, 645–659, https://doi.org/10.5194/acp-7-645-2007, 2007.

Sakai, T., Uchino, O., Nagai, T., Liley, B., Querel, R., Morino, I., Jin, Y., Fujimoto, T., Oikawa, E., and Oshima, N.: Stratospheric aerosol backscatter and depolarization ratio observed with ground–based lidar at Tsukuba, Japan, and Lauder, New Zealand, J. Geophys. Res. Atmos., 130, e2024JD041329, https://doi.org/10.1029/2024JD041329, 2025.

Shang, X., Lipponen, A., Filioglou, M., Sundström, A.-M., Parrington, M., Buchard, V., Darmenov, A. S., Welton, E. J., Marinou, E., Amiridis, V., Sicard, M., Rodríguez-Gómez, A., Komppula, M., and Mielonen, T.: Monitoring biomass burning aerosol transport using CALIOP observations and reanalysis models: a Canadian wildfire event in 2019, Atmos. Chem. Phys., 24, 1329–1344, https://doi.org/10.5194/acp-24-1329-2024, 2024.

Shao, N., Wang, Q., Bu, Z., Yin, Z., Dai, Y., Chen, Y., and Wang, X.: China Aerosol Raman Lidar Network (CARLNET)—Part I: Water Vapor Raman Channel Calibration and Quality Control, Remote Sens., 17, 414, https://doi.org/10.3390/rs17030414, 2025.

Sicard, M., Granados-Muñoz, M. J., Alados-Arboledas, L., et al. Ground/space, passive/active remote sensing observations coupled with particle dispersion modelling to understand the inter-continental transport of wildfire smoke plumes, Remote Sens. Environ., 232, 111294, https://doi.org/10.1016/j.rse.2019.111294, 2019.

Sun, K., Dai, G., Trapon, D., Baars, H., Ansmann, A., Wandinger, U., and Wu, S.: Characterization of aerosol properties during a huge transatlantic smoke transport event using Aeolus observations in synergy with multi-platform data, Atmos. Chem. Phys., 26, 12953–12976, https://doi.org/10.5194/acp-26-12953-2026, 2026.

Trickl, T., Vogelmann, H., Flentje, H., and Ries, L.: Stratospheric ozone in boreal fire plumes – the 2013 smoke season over central Europe, Atmos. Chem. Phys., 15, 9631–9649, https://doi.org/10.5194/acp-15-9631-2015, 2015.

Trickl, T., Vogelmann, H., Fromm, M. D., Jäger, H., Perfahl, M., and Steinbrecht, W.: Measurement report: Violent biomass burning and volcanic eruptions – a new period of elevated stratospheric aerosol over central Europe (2017 to 2023) in a long series of observations, Atmos. Chem. Phys., 24, 1997–2021, https://doi.org/10.5194/acp-24-1997-2024, 2024.

UN: United Nations Environment Programme: Spreading like Wildfire – The Rising Threat of Extraordinary Landscape Fires, edited by: Sullivan, A., Baker, E., & Kurvits, T., UN, https://wedocs.unep.org/handle/20.500.11822/38372 (last access: 24 August 2026), 2022.

van Zadelhoff, G.-J., Donovan, D. P., and Wang, P.: Detection of aerosol and cloud features for the EarthCARE atmospheric lidar (ATLID): the ATLID FeatureMask (A-FM) product, Atmos. Meas. Tech., 16, 3631–3651, https://doi.org/10.5194/amt-16-3631-2023, 2023.

Veselovskii, I., Hu, Q., Ansmann, A., Goloub, P., Podvin, T., and Korenskiy, M.: Fluorescence lidar observations of wildfire smoke inside cirrus: a contribution to smoke–cirrus interaction research, Atmos. Chem. Phys., 22, 5209–5221, https://doi.org/10.5194/acp-22-5209-2022, 2022.

Wang, Y., Cao, Y., Yu, H., Wang, S., Hu, Q., Chang, Y., Zhao, C., Li, Z., and Chen, C.: Wildfire aerosols lofted by North American pyrocumulonimbus clouds: long-range transport and aerosol-cloud-radiative effects, EGUsphere [preprint], https://doi.org/10.5194/egusphere-2025-5076, 2025.

Wehr, T., Kubota, T., Tzeremes, G., Wallace, K., Nakatsuka, H., Ohno, Y., Koopman, R., Rusli, S., Kikuchi, M., Eisinger, M., Tanaka, T., Taga, M., Deghaye, P., Tomita, E., Bernaerts, D.: The EarthCARE mission – Science and system overview, Atmos. Meas. Tech., 16(15), 3581–3608. https://doi.org/10.5194/amt-16-3581-2023, 2023.

Welton, E. J. and Campbell, J. R.: Micropulse lidar signals: Uncertainty analysis, J. Atmos. Ocean. Tech., 19, 2089-2094, https://doi.org/10.1175/1520-0426(2002)019<2089:MLSUA>2.0.CO;2, 2002.

Weng, M., Yi, F., Liu, F., Zhang, Y., and Pan, X.: Single-line-extracted pure rotational Raman lidar to measure atmospheric temperature and aerosol profiles, Opt. Express, 26(21), 27555-27571, https://doi.org/10.1364/OE.26.027555, 2018.

https://doi.org/10.5194/egusphere-2026-6287
Preprint. Discussion started: 10 November 2026
© Author(s) 2026. CC BY 4.0 License.



Wu, X., Qiao, Q., Chen, B., Wang X., Hoffmann L., Griessbach S., Tian Y., and Wang Y.: The influence of the Asian summer monsoon on volcanic aerosol transport in the UTLS region. npj. Clim. Atmos. Sci., 6, 11, https://doi.org/10.1038/s41612-023-00339-w, 2023.

Wu, Z., Seifert, P., He, Y., Baars, H., Li, H., Jimenez, C., Li, C., and Ansmann, A.: Assessment of horizontally oriented ice crystals with a combination of multiangle polarization lidar and cloud Doppler radar, Atmos. Meas. Tech., 18, 3611–3634, https://doi.org/10.5194/amt-18-3611-2025, 2025.

Wu, Z., Li, C., He, Y., Baars, H., and Seifert, P.: Horizontally Oriented Ice Crystals Observed with the Combination of Zenith and 15-degree off-Zenith pointing Polarization Lidar over Beijing (116.3° E 40.0° N), China, EPJ Web Conf., 362, 02021, https://doi.org/10.1051/epjconf/202636202021, 2026a.

Wu, Z., Seifert, P., He, Y., Baars, H., Jimenez, C., Li, C., Li, J., Ansmann, A., and Zhao, C.: Observation-based analysis of horizontally oriented ice crystals using dual-angle polarization lidar and cloud Doppler radar in Beijing, Atmos. Chem. Phys., 26, 11491–11523, https://doi.org/10.5194/acp-26-11491-2026, 2026b.

Xu, X., Jiang, Z., Li, J., Chu, Y., Tan, W., and Li, C.: Impacts of meteorology and emission control on the abnormally low particulate matter concentration observed during the winter of 2017, Atmos. Environ., 225, 117377, https://doi.org/10.1016/j.atmosenv.2020.117377, 2020.

Yi, F., Yu, C., Zhang, Y., Liu, F., Yi, Y., He, Y., Yin, Z., Zhou, J.: Pure rotational Raman lidar for accurate profiling of atmospheric temperature and aerosol/cloud backscatter coefficients, Opt. Express, vol. 32, 45566–45581, https://doi.org/10.1364/OE.539628, 2024

Yi, Y., Yi, F., Liu, F., Zhang, Y., Yu, C., and He, Y.: Microphysical process of precipitating hydrometeors from warm-front mid-level stratiform clouds revealed by ground-based lidar observations, Atmos. Chem. Phys., 21, 17649–17664, https://doi.org/10.5194/acp-21-17649-2021, 2021.

Yin, Z., Yi, F., Liu, F., He, Y., Zhang, Y., Yu, C., and Zhang, Y.: Long-term variations of aerosol optical properties over Wuhan with polarization lidar, Atmos. Environ., 259, 118508, https://doi.org/10.1016/j.atmosenv.2021.118508, 2021.

Zha, C., Bu, L., Li, Z., Wang, Q., Mubarak, A., Liyanage, P., Liu, J., and Chen, W.: Aerosol optical property measurement using the orbiting high-spectral-resolution lidar on board the DQ-1 satellite: retrieval and validation, Atmos. Meas. Tech., 17, 4425–4443, https://doi.org/10.5194/amt-17-4425-2024, 2024.

Zhang, S., Solomon, S., Boone, C. D., and Taha, G.: Investigating the vertical extent of the 2023 summer Canadian wildfire impacts with satellite observations, Atmos. Chem. Phys., 24, 11727–11736, https://doi.org/10.5194/acp-24-11727-2024, 2024.

Zhuang, J. and Yi, F.: Nabro aerosol evolution observed jointly by lidars at a midlatitude site and CALIPSO, Atmos. Environ., 140, 106–116, https://doi.org/10.1016/j.atmosenv.2016.05.048, 2016.